Electric Field-Directed Assembly of Fullerene Crystal Rods into Hierarchical Films

Journal:	*Journal of Materials Chemistry C*
Manuscript ID	TC-ART-05-2018-002363.R1
Article Type:	Paper
Date Submitted by the Author:	14-Sep-2018
Complete List of Authors:	Stelson, Angela; Cornell University, Materials Science and Engineering Penterman, Sonny; Cornell University, Materials Science and Engineering Liddell Watson, Chekesha; Cornell University, Materials Science & Engineering

Electric Field-Directed Assembly of Fullerene Crystal Rods into Hierarchical Films

Angela C. Stelson, Sonny J. Penterman, Chekesha M. Liddell Watson*

Affiliations: Department of Materials Science and Engineering, Cornell University, Ithaca NY 14853

Keywords: self-assembly, electric fields, fullerenes, molecular crystals

**Address correspondence to cml66@cornell.edu*

Abstract

Self-assembly of nanomaterials with desired materials properties requires assembly control from nanometer to millimeter scales. Here, hierarchical C_{60} and C_{70} films are assembled from nanoscale to macroscale by combining co-solvent precipitation with electric-field directed assembly. Fullerene molecular crystals are grown via seeded co-solvent precipitation with mixed organic solvents and antisolvent 2-propanol. Rods of varying aspect ratios (1.7, 2 and 3.7) are prepared as a function of injection volume, fullerene type and solution concentration. Electric fields are applied to colloidal fullerene rods confined to two dimensions. The applied field induces dipolar forces, dielectrophoretic forces, and electrohydrodynamic flows. Frequency-dependent phase transitions occur at the critical Maxwell–Wagner crossover frequency, where the effective polarizability of the particles in the medium is substantially reduced, resulting in changes in structure. Partial order phases form as a function of field strength, frequency, and confinement including tetratic, smectic, centered rectangular and string fluids.

Introduction

Designer colloidal self-assemblies support structure-mediated electronic[1], photonic[2] and mechanical properties[3] that have been applied in photovoltaics[4], color-changing inks[5], catalysis[6], sensing[7] and more. Frequently, these applications require programmable building blocks with properties not typically produced in colloidal synthesis, including semiconducting,[8] magnetic[9] and high dielectric constant materials.[10] Additionally, precise control of microstructure is required, necessitating tight control of inter-particle interactions and local packing. The assembly of building blocks with tunable inter-particle interactions[11–13] and anisotropic shape is key to advancing self-assembly applications as it minimizes further processing required for templating an assembly (e.g. backfilling, sintering and chemically removing the template).[14–16] To date, syntheses that produce electrically functional anisotropic particles with programmable interactions remain scarce, and extending the strategies for building materials at the molecular scale to the assembly of objects at larger scales is being actively pursued in colloid science.[17,18]

A central challenge in designing assemblies with enhanced properties is expanding assembly techniques to generate structures beyond simple close-packed crystals.[19] Anisotropic colloid morphologies expand the range of available structures and symmetries accessible through entropy-driven self-assembly.[12] However, long-range orientational and positional control of anisotropic particles is technically challenging because assembly time scales are longer than spheres, and kinetic traps can prevent ordering.[20] Structural control in self-assembled systems can be enhanced by electric-, magnetic-and flow fields, which direct the interactions between neighboring particles.[21–24] In particular, electric fields applied to colloidal suspensions induce many-body dipolar interactions between particles and produce a wide phase diversity including superlattices, lock-and-key clusters, plastic crystals, tetratic mesophases, etc.[25–30] The combination of multiple assembly effects can further enhance control of particle orientation, order and registry, but generally results in less uniform structures.[31] Understanding the interplay of orthogonal assembly forces in assemblies of anisotropic particles allows us to better control the structure of colloidal solids.

Here, we investigate the impact of confinement and electric fields on the assembly of fullerene molecular crystal rods. Leveraging the interaction of electric fields and two-dimensional confinement enables better control of colloidal film structure (particle alignment and orientation) and produces two-dimensional assemblies beyond thermodynamic equilibrium. Fullerene and functionalized fullerene systems have been proposed for use in photovoltaics,[32] optoelectonic devices,[33–35] and energy storage,[36] but have been limited in macroscale ordering.[33,37,38] By first preparing rod-shaped microcrystals using co-solvent precipitation and subsequently assembling the rods, we achieve hierarchical structures of fullerenes from the nanoscale to the macroscale. We vary the rod aspect ratio and the packing fraction of the molecular crystal rods as well as field strength and frequency. We find that the aspect ratio is critical to the assembly with and without electric fields. A wide range of partial order structures are characterized including tetratic, nematic, smectic A, disordered face-centered rectangular, and string fluids using nematic and tetratic ordering parameters. The frequency dependence of the rod assemblies is described by the Maxwell-Wagner crossover frequency, where a reduction in effective polarizability of the particles changes the assembly dynamics. Notably, the interplay of particle anisotropy and confinement results in distinct phase transitions as a function of electric field frequency.

Results and Discussion

We used scanning electron microscope images to characterize the morphologies, sizes and aspect ratios of fullerene microcrystal rods used in directed assembly studies (Fig. 1, Table 1). All particles are identified by their fullerene chemistry and aspect ratio (e.g. a C_{60} particle with and aspect ratio of two is referred to as C_{60}-2). The C_{60} rods were synthesized using co-solvent precipitation with mixed good solvent, i.e., tetralin (THN) as the good solvent and 2,4,6 trimethylpyridine (TMP) as a structure directing agent.[39] Figure 1 (a-b) displays these rods which have hexagonal faceting and aspect ratios of 2 and 1.7 respectively, which were prepared from 200 μL and 300 μL injection volume of 80:20 THN/TMP, respectively. The particles are denoted C_{60}-2 and C_{60}-1.7 based on their composition and aspect ratio. [39] The C_{70} microcrystals synthesized with 200 μL injection volume of mesitylene (C_{70}-3.9) displayed in Fig. 1(c) have an aspect ratio of 3.9 and are not strongly faceted. Defects in particle morphology consisted primarily of broken particles, although branched crystal particles occurred rarely in the C_{60} particle systems. The length, width and aspect ratios of all three particles (Table 1), were calculated from SEM images. All three particles display a polydispersity index (PDI) approaching unity, indicating a narrow distribution of particle sizes.

The assembly of the fullerene rods under two-dimensional confinement without electric field is shown in Figure 2. The particles are injected into a wedge-shaped confinement cell and driven to the bottom by slow centrifugation over several hours, then imaged with an optical microscope *in situ* (transmission mode). The C_{60}-2 rods [Fig. 2(a)] form a tetratic mesophase with long range order, as confirmed by the Fast Fourier Transform (FFT) image in the inset which displays orientational ordering (four-fold symmetric sharp ring patterns). Previous theoretical work has predicted the formation of a tetratic mesophase for two-dimensional assemblies of dominos.[40–42] However, true tetratic structures have been technically difficult to achieve due to their sensitivity to particle aspect ratio and degree of faceting, and have not been observed in assemblies of rods as predicted.[43,44] Local tetratic packing is also present in the assembly of C_{60}-1.7 particles [Fig. 2(b)] as indicated by the inset FFT. The C_{70}-3.9 rods pack into clusters of rods, and the orientation of these stacks does not have a long-range orientational correlation, resulting in an isotropic FFT pattern. We calculated the orientational order parameter S_{2m} to characterize the overall nematic (S_2) and tetratic ordering (S_4) (see Table 2). The order parameter is calculated as $S_{2m} = \langle \cos(2m\theta) \rangle$ where θ is the angle between a particle and the local director. The surface coverage for each assembly was calculated using the dimensions calculated from SEM images and the particle counts from optical micrographs (Table 2). The surface coverage of the C_{60}-2 rods was highest (70%), which was in good agreement with the high degree of ordering in that assembly (S_4 = 0.76).

The orientational correlation function $g_{2m}(r)$ is used to characterize the long-range tetratic ordering of the fullerene microcrystal rods. The correlation functions plotted in Figure 3(a-c) were calculated from particle positions and orientations determined from representative micrographs covering between 1600 to 3200 μm^2. The correlation function is given by $g_{2m}(r) = \langle cos\{2m[\theta(0) - \theta(r)]\} \rangle$, where m = 1, 2, 3 corresponds to nematic, tetratic, and hexatic order.

For a given angular symmetry (m = 1, 2, etc.) correlation values approaching one correspond to higher correlation, whereas values approximately equal to zero indicate no correlation along those angles. The higher order correlation $g_8(r)$ (m = 4) is used as a secondary indicator of tetratic ordering with higher sensitivity to angular misorientation.[43] The correlation functions $g_4(r)$ and $g_8(r)$ in Figure 3(a) demonstrate long range correlation in the C_{60}-2 system, confirming large regions of tetratic ordering. The faster decay of $g_8(r)$ occurs due to its high angular sensitivity, and the rapid decay of $g_2(r)$ and $g_6(r)$ indicate a lack of 2-fold and 6-fold symmetric ordering. The nearest neighbor distance, given by the peak in $g_{2m}(r)$, is 0.95 μm, larger than the shortest dimension of the particle (0.61 μm). This indicates an average spacing between C_{60}-2 particles of approximately 0.34 μm.

The C_{60}-1.7 system [Fig. 3(b)], displays a rapid decay of all the correlation functions, indicating orientational disorder. The tetratic correlation function only shows correlation to the second-nearest neighbor, indicating only small, weakly correlated regions. While long-range tetratic order was not observed in this system, clusters of tightly packed and aligned rods were observed, in line with Monte Carlo simulations of high aspect ratio rods.[44] The nearest neighbor distance in the C_{60}-1.7 system is 1.0 μm, yielding an average interparticle distance of 0.16 μm, indicating a smaller interparticle spacing than the C_{60}-2 particles.

The orientational correlations displayed in Fig. 3(c) for the C_{70}-3.9 rods indicate only tetratic ordering within the nearest neighbors. The nearest neighbor distance for the C_{70}-3.9 rods was 0.35 μm with an average interparticle spacing of approximately 60 nm. This close packing between the rods is supported by the much higher surface coverage values for the C_{70}-3.9 films

(80%). The decay of both the C_{60}-1.7 and the C_{70}-3.9 assemblies occurs roughly at the aspect ratios of the particles, These results agree well with a wide range of theoretical studies, which predict that strong faceting (C_{60}-1.7) and longer aspect ratios (C_{70}-3.9) lead to weaker tetratic correlations.[40,41,44]

In self-assembled systems, the applications of an alternating current (AC) fields produces a frequency-dependent dipolar response in the particles, and modifies the interactions between particles.[1,45] In the kHz to MHz frequency range, the dominant frequency-dependent phenomenon in particle suspensions is the Maxwell-Wagner interfacial relaxation.[46] The interface between particle and medium produces a charge build-up with a characteristic dipole and corresponding dipolar relaxation time. The crossover frequency is the frequency at which the particle transitions from being polarized in one direction with respect to the field (e.g., along the field), to the opposite direction (e.g. against the electric field). The frequency dependence of the effective polarizability of fullerene microcrystals in the solvent, is determined by the real component of the Clausius-Mossotti factor ($Re|K(\omega)|$) for ellipsoidal particles, where—

$$K_\alpha(\omega) = \frac{\varepsilon_p^* - \varepsilon_s^*}{3(\varepsilon_s^* + (\varepsilon_p^* - \varepsilon_s^*)L_\alpha)}, \qquad (1)$$

where α is a dimensions x and y, which correspond to the directions of the major and minor axes of the rod, respectively. The parameters L_x and L_y are

$$L_x = \frac{a^2 b}{2} \int_0^\infty \frac{ds}{(s+a^2)\sqrt{(s+b^2)(s+a^2)^2}}$$

and

$$L_y = \frac{a^2 b}{2}\int_0^\infty \frac{ds}{(s+b^2)\sqrt{(s+b^2)(s+a^2)^2}},$$

where a and b correspond to the minor and major axes of the dimensionally equivalent ellipse. The complex permittivity is $\varepsilon^* = \varepsilon - \frac{i\sigma}{\omega}$ where ε is the dielectric constant, σ is the loss and ω is the frequency of the applied field.[1,47] The subscripts of ε_p^* and ε_s^* refer to the particle and solvent, respectively. The observed crossover frequency f_c is proportional to the inverse of the Maxwell-Wagner relaxation time $\tau_{MW} = \frac{\sqrt{3}(\varepsilon_p + L_\alpha(\varepsilon_p - \varepsilon_s))}{\sigma_p + L_y(\sigma_p - \sigma_s)}$. The characteristic relaxation associated with the minor axis is predicted to occur at much higher frequencies the ones used in this study. At the frequency f_c, the effective polarization of the particle in the medium sharply decreases in magnitude and we expect the system to demonstrate a transition in self-assembly behavior. The dipole moment within a rod can be estimated as—[48]

$$\boldsymbol{p_\alpha} = 4\pi^2 a^2 b \varepsilon_s \varepsilon_o K_\alpha(\omega) \boldsymbol{E_\alpha} \tag{2}$$

For the calculation of $K_\alpha(\omega)$, the fluid values were measured and the static dielectric constant for C_{60} and C_{70} from reference [49] was used. We used a range of conductivity from the literature as the conductivity of fullerene crystals is highly dependent on oxygen content, impurities and crystal structure.[49–51] The dipole moment of the rods used in these assemblies are anti-parallel with the applied field at all frequencies for reported properties of fullerene molecular crystals, but still display a crossover frequency where the magnitude of the dipole is reduced.[28] We calculated the orientational order parameter P_2 that quantifies the alignment of particles with respect to the field (P_2 = 1 corresponds to alignment along the field, while P_2 = -1 corresponds to alignment perpendicular to the field and P_2 = 0 corresponds to random alignment). The order parameter P_2 is defined as:

$$P_2 = \int_0^{\pi/2} \frac{\exp(-\frac{U(\theta)}{kT})}{\int_0^{\pi/2} \exp(-\frac{U(\theta)}{kT}) d\theta} cos2\theta d\theta \qquad (3$$

where $U(\theta)$ is the energy of an polarized ellipsoid under an electric field:

$$U(\theta) = -A\, Re(\boldsymbol{p} \cdot \boldsymbol{E}). \qquad (4)$$

The P_2 parameters for all three particle geometries are greater than zero for frequencies above and below f_c, meaning that the particles align, on average, along the electric field at all frequencies measured here. The Clausius-Mossotti relationship has been applied in a variety of anisotropic particle systems and assumes an internal electric field parallel to the applied field.[52,53] We expected dielectrophoretic forces along the gradient of the electric field to play a negligible role in these assemblies of the rods they are confined to the plane of the electrode.[1] Moreover, the self- and directed assembly of the fullerene rods were studied more than 20 μm from the electrode, where edge field gradient effects are negligible.

We assembled fullerene hierarchical films under two-dimensional confinement and electric field over a range of area fractions (Fig. 4) and characterized their order (Fig. 5, Table 2). A field **E** with frequency below the crossover frequency f_c (1.8-2.4 MHz) was applied to induce dipolar interactions between the particles. For high area fraction in the C_{60}-2 assembly [Fig. 4(a)], tetratic ordering was re-oriented so that the director pointed along the electric field, and gaps formed as particles exhibited chaining behavior parallel and perpendicular to the applied field. The increased tetratic ordering parameter S_4 (0.82), and higher $g_4(r)$ and $g_8(r)$ correlation functions showed that the electric field induced increased long-range ordering in the assembly while not affecting the overall surface coverage. As the area fraction is decreased [Figs. 4(b,c)] the rods oriented preferentially along the electric field in chains, with a smaller proportion of particles oriented perpendicular to the field. Rods with perpendicular orientation occurred where chains coalesced and act as bridges between chains. The S_2 and S_4 values increased as the overall area coverage is decreased, and the $g_{2m}(r)$ showed longer range orientational correlation for lower surface coverage, as expected. The nearest neighbor distance increased for all C_{60}-2 assemblies with $f < f_c$ to 1.4 μm, indicative of the dominant head-to-tail configuration of particles under applied field. While the field-induced smectic phases and string fluids has been observed in three-dimensional systems, [54] tetratic phases have not been predicted or observed under electric field in bulk systems.[55]

Assemblies of C_{60}-1.7 rods [Figs. 4(d-f)] were generally less well ordered and more nematic than those for C_{60}-2.0. At high area fraction, the structure displayed some nematic character oriented along the electric field, as indicated by the FFT, though the $g_{2m}(r)$ calculations did not show long-range orientational ordering. The S_2 and $g_2(r)$ order parameters increased with decreasing area fraction, indicating a transition from disorder to the nematic phase. At lower area fractions [Figs. 4(e, f)], the C60-1.7 rods preferentially re-oriented themselves with the field and chain, but the resulting chains were on average much shorter than those in the C_{60}-2 assemblies, suggesting that a reduction in anisotropy diminished chaining interactions between the rods.

At high and intermediate area fraction [Fig. 4(g)], the C_{70}-3.9 rods formed smectic liquid crystal grains oriented along the electric field, as indicated by the FFT, S_2 and $g_2(r)$ parameters. By applying an electric field, we enhanced the ordering of the C_{70}-3.9 films while maintaining high coverage (area fractions up to 0.89), making these films appealing for photonic applications.[20] At low area fraction, C_{70}-3.9 rod assemblies transitioned from smectic regions with larger interparticle spacing [Fig. 4(h)] to string fluids [Fig. 4(i)]. Generally, increasing the particle anisotropy increased particle chaining effects, in agreement with theoretical predictions.[52] The characteristic angle θ_c between neighboring C_{70}-3.9 rods in the string fluids was approximately 7 ° off from head-to-tail, distinct from the C_{60} string fluid assemblies, where we observed 0 ° characteristic angle (head-to-tail chaining). Chain formation at characteristic angles has been observed in assemblies of ellipsoids under field,[56] whereas head-to-tail chaining occurs in faceted polyhedral particles. [29,57] Facets, particularly on the ends of the rods, are more clearly defined in the C_{60} systems, and this may account for the difference in chaining behavior. Notably, the observed characteristic angle for C_{70}-3.9 rods was lower than predicted for an ellipse with equivalent aspect ratio (20 ° to 25 °)[56] demonstrating that approximating the C_{70}-3.9 rods as an ellipse does not fully capture their chaining behavior.

At frequencies above f_c, the magnitude of the effective polarization of the particle is decreased, and electrohydrodynamic flows are induced.[28] These flows push the rods toward the electrode edges, typically resulting in dense assemblies. We assembled rods above the crossover frequency f_c (Fig. 6) and calculated the $g_{2m}(r)$ functions (Fig. 7). Both the C_{60}-2 and the C_{60}-1.7 rods formed well-ordered smectic phases oriented along the electric field, as shown by the FFTs and the $g_2(r)$ functions. The C_{60}-2 system displays a mixture of smectic A and disordered face-centered rectangular, while the C_{60}-1.7 rods form exclusively smectic A. In contrast, the C_{70}-3.9 particles form a non-close-packed assembly in a mixture of centered rectangular configurations. Two registries between the rods are common (close-packed centered rectangular with θ_c = 70 °, and a spaced out 'fishnet' structure θ_c = 22 °), suggesting two interparticle dipolar configurations with similar energies. The θ_c for the 'fishnet' centered rectangular structure is similar to the predicted angle of an ellipsoid under field, but no secondary characteristic angle has been observed in ellipsoid assemblies under field. Monte Carlo double-charge simulations of rods with aspect ratios of 5.0 in three dimensions have predicted staggered rod configurations under electric fields, but only a single staggered configuration was predicted.[54]

Conclusion

In this report, we demonstrate the assembly of fullerene molecular crystal rods into two-dimensional hierarchically-ordered macroscale films. These structures bypass the need for further processing for electronic and photonic applications because of the optoelectronic properties inherent to the fullerene building blocks. By varying the aspect ratio of the rods, we achieve a wide phase diversity as a function of filling fraction and field frequency including tetratic, smectic, disordered face-centered rectangular, and string fluids. Combining multiple assembly effects such as two-dimensional confinement and electric fields is a promising means to generate diverse structures. The phase behavior of the fullerene rods under field suggests that further theory is required to understand frequency-dependent response in confined anisotropic particle systems to account for excluded volume and particle geometry effects.

Acknowledgements

The authors would like to thank Abby R. Goldman for assistance in scanning electron micron imaging. This work was supported by the NSF Division of Materials Research under award Grant No. 1508592. The facilities used in this work were funded by NSF under Agreements DMR-0520404, DMR-1120296, and DMR-1719875 as well as ECS-0335765 and ECS-9876771.

Methods

The synthesis of the C_{60} and C_{70} fullerene microcrystals has been described elsewhere in detail.[39,58] In particular, a 10 mL aliquot of 2-propanol (Sigma-Aldrich, >99.8%) in a 20 mL scintillation vial was stirred on a magnetic stirrer plate at 500 rpm. For the C60 rods, fullerene C60 (Sigma-Aldrich, >99.9%) was dissolved in 80:20 tetralin [(1,2,3,4-tetrahydronaphthalene), Sigma-Aldrich, 99%]/ [(2,4,6 trimethylpyridine), Sigma-Aldrich, 99%] in an ultrasonic bath to produce a with a 1.8 mM fullerene concentration. The good solvent mixture was delivered via micropipette (200 μL injection volume for C_{60}-2, 300 μL injection volume for C_{60}-1.7) into the alcohol and stirring continued for a few seconds until the onset of fullerene crystal nucleation was indicated by color change. Stirring was continued for up to 10 s after color change, then removed from the stir plate. The solution was left uncapped to evaporate the excess alcohol over 5–48 h. The C_{70}-3.7 rods were similarly prepared in a 100% mesitylene solvent [(1,3,5-trimethylbenzene), Sigma-Aldrich, >98%] with a 0.7 mM fullerene concentration and 200 μL injection volume. The anisotropy and optical absorption properties of these particles do not allow for many standard particle-counting metrologies such as dynamic light scattering. Instead, the particle concentration in solution were counted using automated image analysis of a random sampling of microscope images. A known volume (10 μL of sample) was pipetted onto a cover slip of known area (20 mm x 20 mm) to construct a 'slice' of liquid where all particles were visible with backlit illumination. Particles were counted over 100 images with 1600 µm2 surface coverage, and the known thickness of fluid volume was used to calculate the average particle concentration.

Fullerene rods were tumbled in 2.3 mM solution of 40,000 MW Polyvinylpyrrolidone (Sigma Aldrich) in isopropanol overnight to prepare them for assembly. The fabrication of confinement cells has been described in detail elsewhere.[28] A 20 µL aliquot of particle solution (concentration 2 x 10^8/mL) was filled into the cell. The cell opening was wrapped with Parafilm to prevent leaking and evaporation. Cells were centrifuged in a custom-built holder at 1500 rpm for 2-6 hours. Centrifugation was required to densify the particles at the bottom of the cell, and centrifugation rate was not found to affect the structure of the assembly.

Confinement cells were imaged using a BX-51 Olympus microscope in bright field transmission mode at 100x magnification. Leads were attached to the electrodes using lead-tin solder, and fields were applied using a function generator (Tektronix), and a wide-band power amplifier (Krohn-Hite Corp. 7602M). Electric fields were applied for 2-6 minutes for low-frequency experiments, with periods of 1-5 minutes between experiments. In these periods, short pulses of low voltage and frequency fields (2 Hz, 2.6 kV/cm) were utilized to induce oscillatory osmotic currents that returned particle disorder to the system. Electric fields were applied in order of increasing frequency. Assembly was observed more than 20 µm from the electrode edge to avoid regions with strong electric field gradients.

The crossover frequency was empirically determined by examining the electrode edge and observing the particle behavior transition from attractive to repulsive with respect to the electrode. The crossover frequency (f_c) observed was 1.8 MHz (C_{60}) and 2.6 MHz (C_{70}) (+/- 0.1

MHz) for field strength 5.4 kV/cm. The static dielectric constant of the medium was measured as 1.7 x 10-12 F/cm using a coaxial dip probe and an LCR meter. We calculated the conductivity of the medium by observing the crossover frequency of commercially available polystyrene colloids (Duke Scientific). Specifically, we combined particle dielectric constant values from the literature[59] with our static dielectric constant measurements of the medium using the equation for the Maxwell-Wagner relaxation time. The conductivity of the medium was predicted to be 1.75 x 10-6 S/cm at field strength of 5.4 kV/cm. ImageJ was used to process images and produce fast Fourier transforms (FFTs). Matlab graphical input was used to calculate the radial distribution functions and orientational correlation functions.

References

1 O. D. Velev, in *Colloids and Colloid Assemblies*, ed. F. Caruso, 2004, pp. 437–464.

2 J. F. Galisteo-López, M. Ibisate, R. Sapienza, L. S. Froufe-Pérez, A. Blanco and C. López, *Adv. Mater.*, 2011, **23**, 30–69.

3 Y. D. Liu and H. J. Choi, *Soft Matter*, 2012, 11961–11978.

4 A. Mihi, F. J. López-Alcaraz and H. Míguez, *Appl. Phys. Lett.*, 2006, **88**, 193110.

5 H. Fudouzi and Y. Xia, *Adv. Mater.*, , DOI:10.1002/adma.200304795.

6 M. Sauer and W. Meier, 2004, 150–174.

7 S. A. Asher, S. F. Peteu, C. E. Reese, M. X. Lin and D. Finegold, *Anal. Bioanal. Chem.*, 2002, **373**, 632–638.

8 J. E. Wijnhoven, *Science (80-.).*, 1998, **281**, 802–804.

9 S. H. Lee and C. M. Liddell, *Small*, 2009, **5**, 1957–62.

10 R. Fenollosa, F. Meseguer and M. Tymczenko, *Adv. Mater.*, , DOI:10.1002/adma.200701589.

11 S. Gangwal, A. Pawar, I. Kretzschmar, O. D. Velev, Velev and O. D., *Soft Matter*, 2010, **6**, 1413.

12 F. a Escobedo, *Soft Matter*, 2014, **10**, 8388–400.

13 G. van Anders, D. Klotsa, N. K. Ahmed, M. Engel and S. C. Glotzer, *Proc. Natl. Acad. Sci.*, ,

DOI:10.1073/pnas.1418159111.

14 Z.-Y. Li and Z.-Q. Zhang, *Phys. Rev. B*, 2000, **62**, 1516.

15 T. Ruhl, P. Spahn, C. Hermann, C. Jamois and O. Hess, *Adv. Funct. Mater.*, 2006, **16**, 885–890.

16 R. G. Shimmin, R. Vajtai, R. W. Siegel and P. V. Braun, *Chem. Mater.*, 2007, **19**, 2102–2107.

17 P. F. Damasceno, M. Engel and S. C. Glotzer, *Science*, 2012, **337**, 453–7.

18 S. C. Glotzer and M. J. Solomon, *Nat. Mater.*, 2007, **6**, 557–562.

19 F. Meseguer, *Colloids Surfaces A Physicochem. Eng. Asp.*, 2005, **270**, 1–7.

20 M. J. Solomon, *Curr. Opin. Colloid Interface Sci.*, 2011, **16**, 158–167.

21 A. F. Demirörs, P. M. Johnson, C. M. van Kats, A. van Blaaderen and A. Imhof, *Langmuir*, 2010, **26**, 14466–71.

22 a. Blaaderen, M. Dijkstra, R. Roij, A. Imhof, M. Kamp, B. W. Kwaadgras, T. Vissers and B. Liu, *Eur. Phys. J. Spec. Top.*, 2013, **222**, 2895–2909.

23 M. Golosovsky, Y. Saado and D. Davidov, *Appl. Phys. Lett.*, 1999, **75**, 4168.

24 B. Sun and H. Sirringhaus, *J. Am. Chem. Soc.*, 2006, **128**, 16231–16237.

25 W. Ristenpart, I. Aksay and D. Saville, *Phys. Rev. Lett.*, 2003, **90**, 128303.

26 M. Kamp, N. A. Elbers, T. Troppenz, A. Imhof, M. Dijkstra, R. van Roij and A. van Blaaderen, *Chem. Mater.*, 2016, acs.chemmater.5b04152.

27 B. Liu, T. H. Besseling, M. Hermes, A. F. Demirörs, A. Imhof and A. van Blaaderen, *Nat. Commun.*, 2014, **5**, 3092.

28 A. C. Stelson, S. J. Penterman and C. M. L. Watson, *Small*, 2017, **1603509**, 1603509.

29 H. R. Vutukuri, F. Smallenburg, S. Badaire, A. Imhof, M. Dijkstra and A. van Blaaderen, *Soft Matter*, 2014, **10**, 9110–9119.

30 A. A. Shah, H. Kang, K. L. Kohlstedt, K. H. Ahn, S. C. Glotzer, C. W. Monroe and M. J. Solomon, *Small*, 2012, **8**, 1551–1562.

31 A. H. Gröschel and A. H. E. Müller, *Nanoscale*, 2015, **7**, 11841–11876.

32 M. Bernardi, J. Lohrman, P. V. Kumar, A. Kirkeminde, N. Ferralis, J. C. Grossman and S. Ren, *ACS Nano*, , DOI:10.1021/nn302893p.

33 S. Zheng, M. Xu and X. Lu, *ACS Appl. Mater. Interfaces*, 2015, **7**, 20285–20291.

34 X. Jiang, M. Yuan, H. Liu, L. Liubang and Z. Du, *Mater. Lett.*, 2016.

35 X. X. Liao, T. Wang, J. Wang, J. C. Zheng, C. Wang and V. W. W. Yam, *ACS Appl. Mater. Interfaces*, , DOI:10.1021/am402523n.

36 J. Chen and F. Wu, *Appl. Phys. A Mater. Sci. Process.*, 2004.

37 P. Bairi, K. Minami, W. Nakanishi, J. P. Hill, K. Ariga and L. K. Shrestha, *ACS Nano*, 2016, **10**, 6631–

6637.

38 A. Aggeli, I. A. Nyrkova, M. Bell, R. Harding, L. Carrick, T. C. B. McLeish, A. N. Semenov and N. Boden, *Proc. Natl. Acad. Sci.*, 2001, **98**, 11857–11862.

39 S. J. Penterman and C. M. Liddell Watson, *CrystEngComm*, 2016, **18**, 1775–1781.

40 J. Geng and J. V. Selinger, *Phys. Rev. E - Stat. Nonlinear, Soft Matter Phys.*, 2009, **80**, 1–6.

41 A. Donev, J. Burton, F. H. Stillinger and S. Torquato, *Phys. Rev. B - Condens. Matter Mater. Phys.*, 2006, **73**, 1–11.

42 V. Narayan, N. Menon and S. Ramaswamy, *J. Stat. Mech. Theory Exp.*, , DOI:10.1088/1742-5468/2006/01/P01005.

43 K. Zhao, C. Harrison, D. Huse, W. B. Russel and P. M. Chaikin, *Phys. Rev. E - Stat. Nonlinear, Soft Matter Phys.*, 2007, **76**, 1–4.

44 Y. Martínez-Ratón and E. Velasco, *Phys. Rev. E - Stat. Nonlinear, Soft Matter Phys.*, , DOI:10.1103/PhysRevE.79.011711.

45 M. L. Jim??nez and T. Bellini, *Curr. Opin. Colloid Interface Sci.*, 2010, **15**, 131–144.

46 K. Asami, *Prog. Polym. Sci.*, 2002, **27**, 1617–1659.

47 L. Csoka, I. C. Hoeger, P. Peralta, I. Peszlen and O. J. Rojas, *J. Colloid Interface Sci.*, 2011, **363**, 206–212.

48 M. Mittal and E. M. Furst, *Adv. Funct. Mater.*, 2009, **19**, 3271–3278.

49 A. F. Hebard, R. C. Haddon, R. M. Fleming and A. R. Kortan, *Appl. Phys. Lett.*, 1991, **59**, 2109–2111.

50 B. Pevzner and A. Hebard, *Phys. Rev. B - Condens. Matter Mater. Phys.*, , DOI:10.1103/PhysRevB.55.16439.

51 H. X. Ji, J. S. Hu, L. J. Wan, Q. X. Tang and W. P. Hu, *J. Mater. Chem.*, 2008, **18**, 328–332.

52 B. W. Kwaadgras, M. Dijkstra and R. Van Roij, *J. Chem. Phys.*, , DOI:10.1063/1.3701615.

53 B. W. Kwaadgras, M. Verdult, M. Dijkstra and R. Van Roij, *J. Chem. Phys.*, , DOI:10.1063/1.3637046.

54 A. Kuijk, T. Troppenz, L. Filion, A. Imhof, R. van Roij, M. Dijkstra and A. van Blaaderen, *Soft Matter*, 2014, **10**, 6249–6255.

55 A. Kuijk, D. V. Byelov, A. V. Petukhov, A. Van Blaaderen and A. Imhof, *Faraday Discuss.*, , DOI:10.1039/c2fd20084h.

56 J. P. Singh, P. P. Lele, F. Nettesheim, N. J. Wagner and E. M. Furst, *Phys. Rev. E. Stat. Nonlin. Soft Matter Phys.*, 2009, **79**, 050401.

57 N. Yanai, M. Sindoro, J. Yan and S. Granick, *J. Am. Chem. Soc.*, 2013, **135**, 34–37.

58 S. J. Penterman, A. Singh, W. R. Zipfel and C. M. Liddell Watson, *Adv. Opt. Mater.*, 2014, **2**, 1024–1030.

59 S. Gangwal, O. J. Cayre and O. D. Velev, *Langmuir*, 2008, **24**, 13312–13320.

Tables and Figures

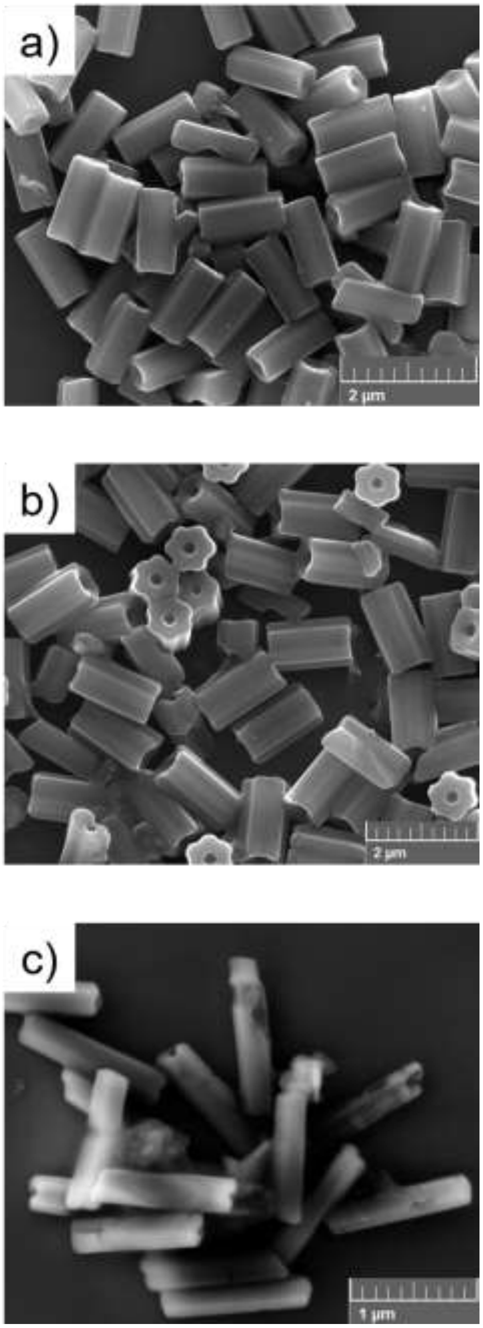

Figure 1: SEM Images of fullerene microcrystal rods a) C_{60}-2 rods, b) C_{60}-1.7 rods and c) C_{70}-3.9 rods.

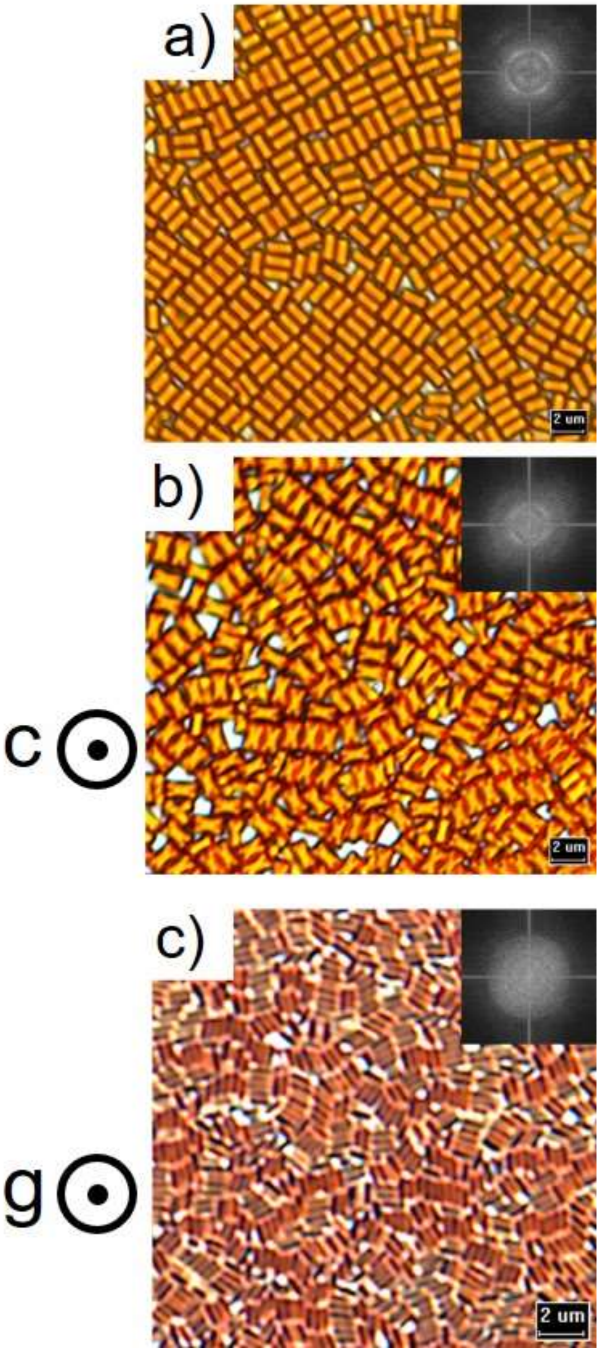

Figure 2: Assembly of fullerene microcrystal rods under two-dimensional confinement. a) C_{60}-2 rods, b) C_{60}-1.7 rods and c) C_{70}-3.9 rods.

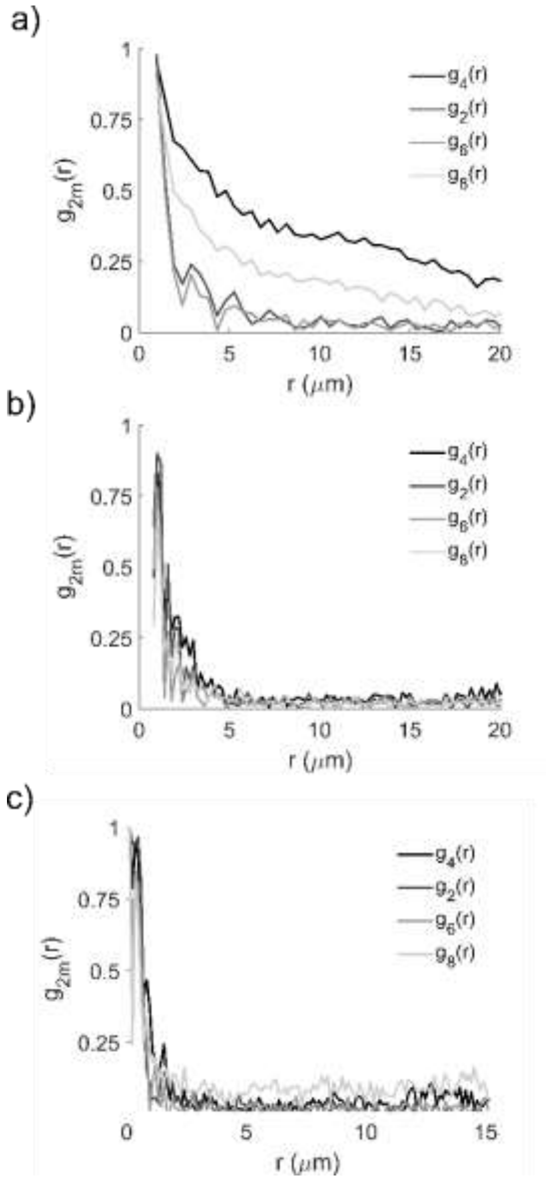

Figure 3: Orientational correlation functions g2m(r) for assemblies of fullerene microcrystal rods under two-dimensional confinement. a) C_{60}-2 rods, b) C_{60}-1.7 rods and c) C_{70}-3.9 rods.

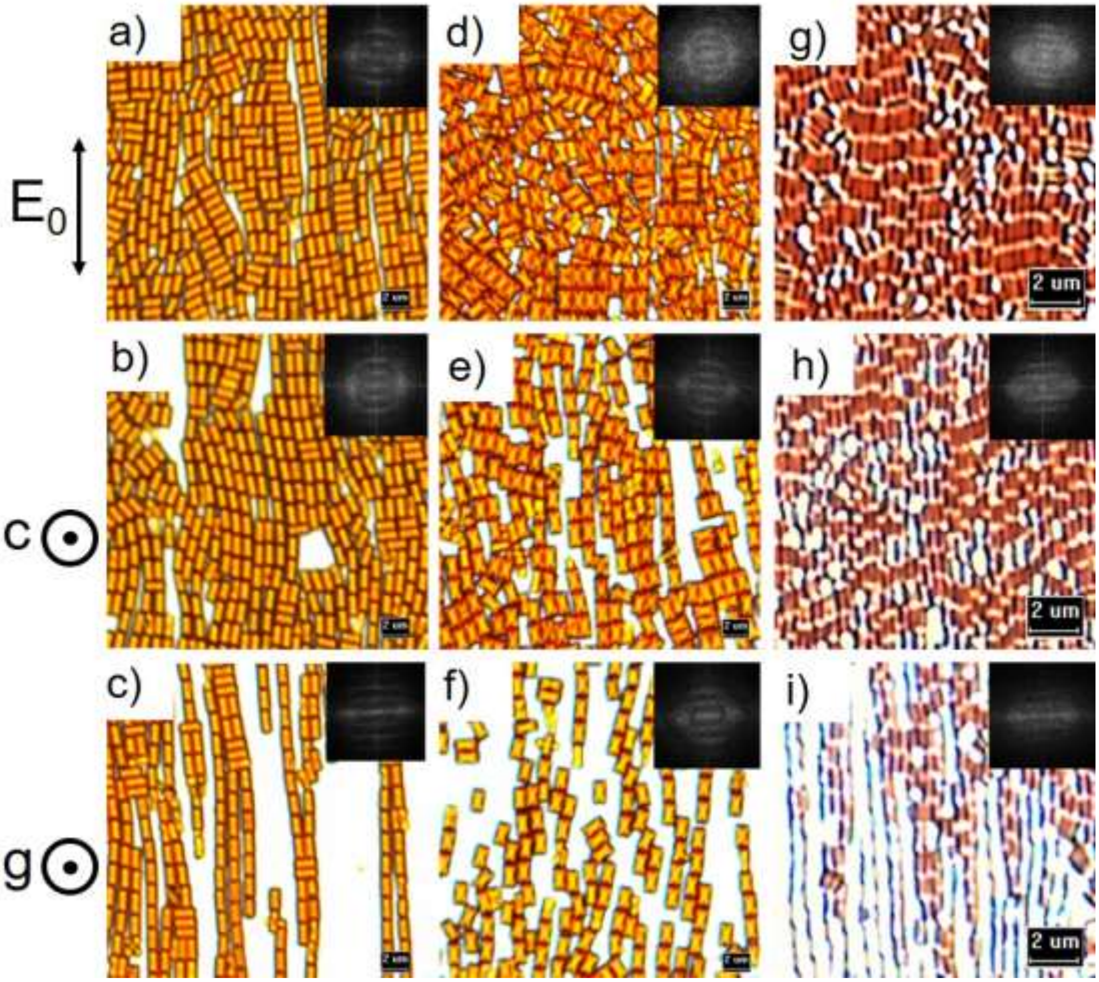

Figure 4: Assemblies of fullerene microcrystal rods under two-dimensional confinement and electric field frequency below f_c. a-c) C_{60}-2 rods assembled at 10kHz, 4kV/cm for a) high area fraction, b) intermediate area fraction, c) low area fraction. d-f) C_{60}-1.7 rods assembled at 10kHz, 4kV/cm for d) high area fraction, e) intermediate area fraction, f) low area fraction. g-i) C_{70}-3.9 rods assembled at 10kHz, 5.3kV/cm for g) high area fraction, h) intermediate area fraction, i) low area fraction.

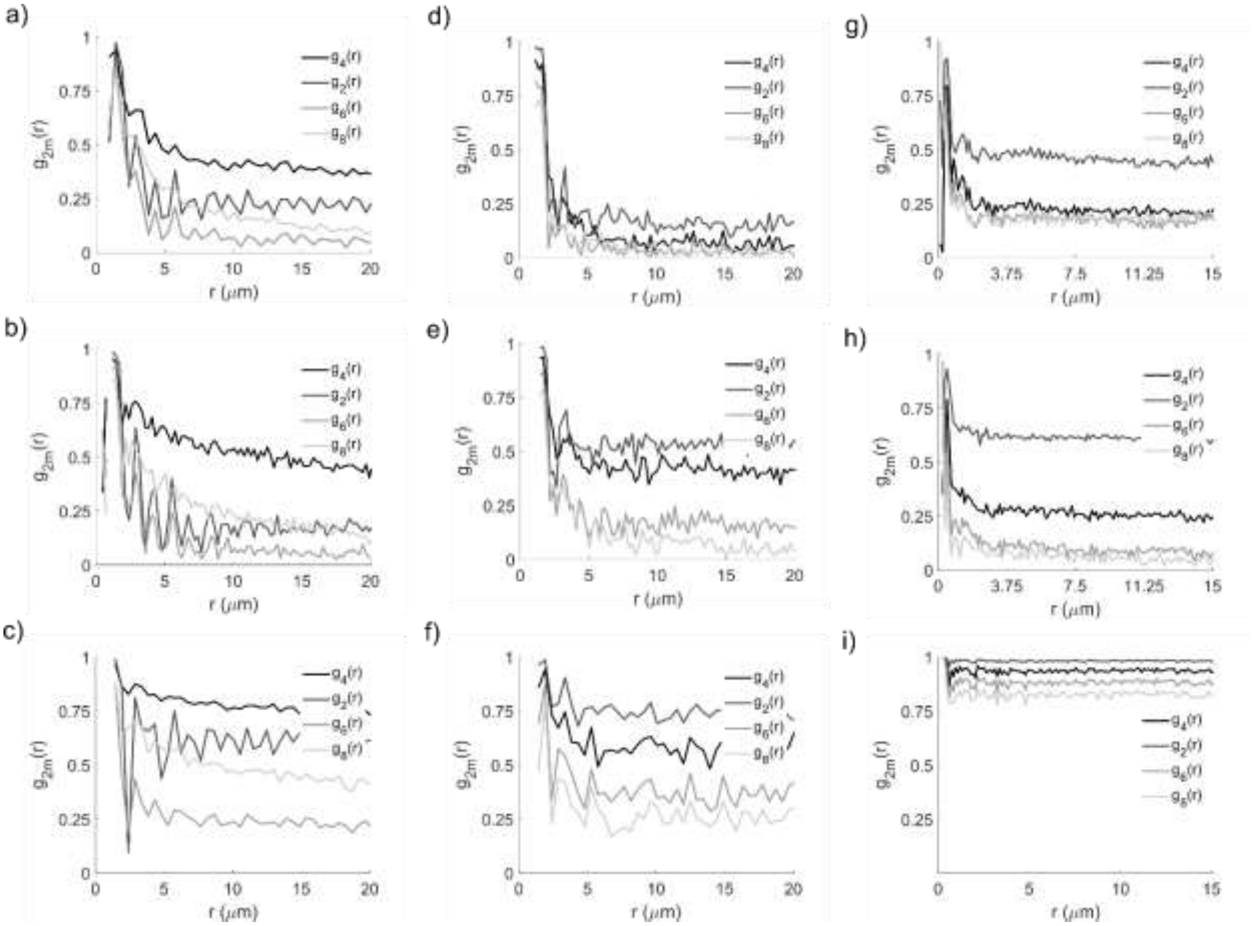

Figure 5: Orientational correlation functions g2m(r) for assemblies of fullerene microcrystal rods under two-dimensional confinement and electric field frequency greater than *f_c*. a) C_{60}-2 under two-dimensional confinement and electric field frequency below f_c. a-c) C_{60}-2 rods assembled at 10kHz, 4kV/cm for a) high area fraction, b) intermediate area fraction, c) low area fraction. d-f) C_{60}-1.7 rods assembled at 10kHz, 4kV/cm for d) high area fraction, e) intermediate area fraction, f) low area fraction. g-i) C_{70}-3.9 rods assembled at 10kHz, 5.3kV/cm for g) high area fraction, h) intermediate area fraction, i) low area fraction.

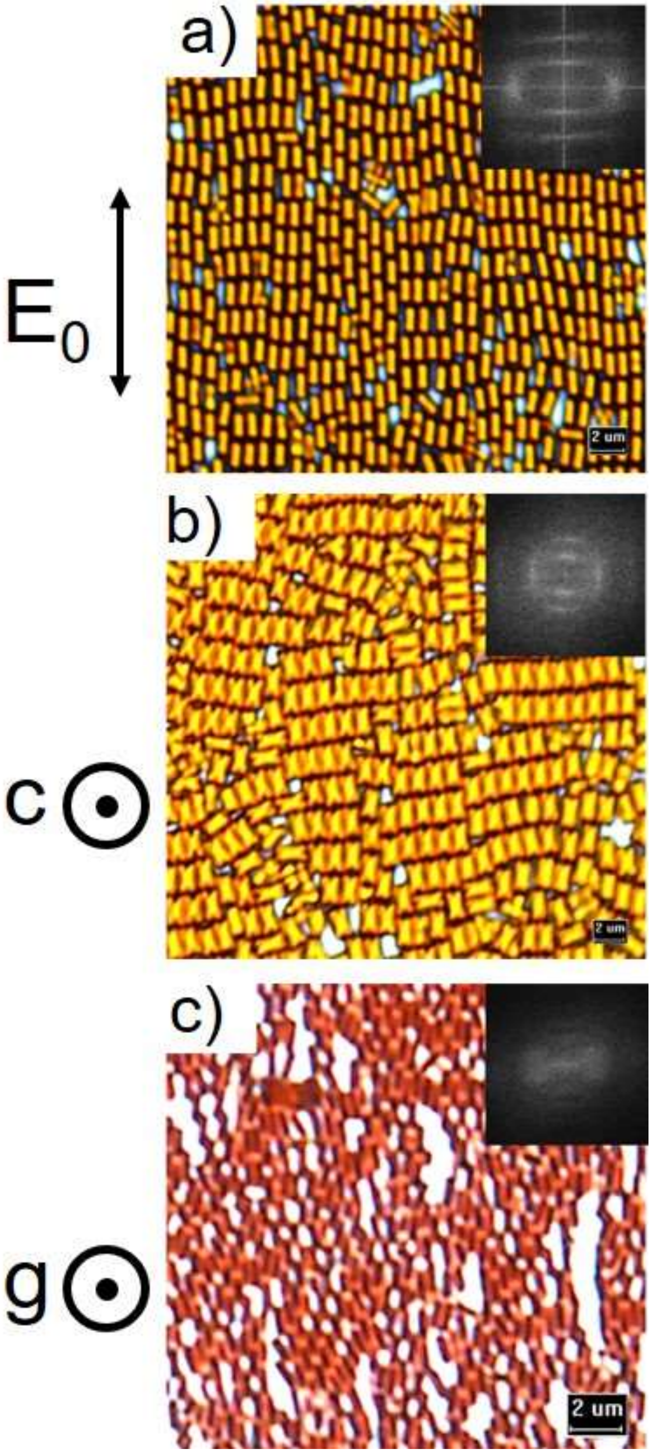

Figure 6: Assemblies of fullerene microcrystal rods under two-dimensional confinement and electric field frequency greater than f_c. a) C_{60}-2 rods assembled at 3 MHz, 1.36 kV/cm, b) C_{60}-1.7 rods assembled at 3 MHz, 1.36 kV/cm, and c) C_{70}-3.9 rods assembled at 3.1 MHz, 1.23 kV/cm.

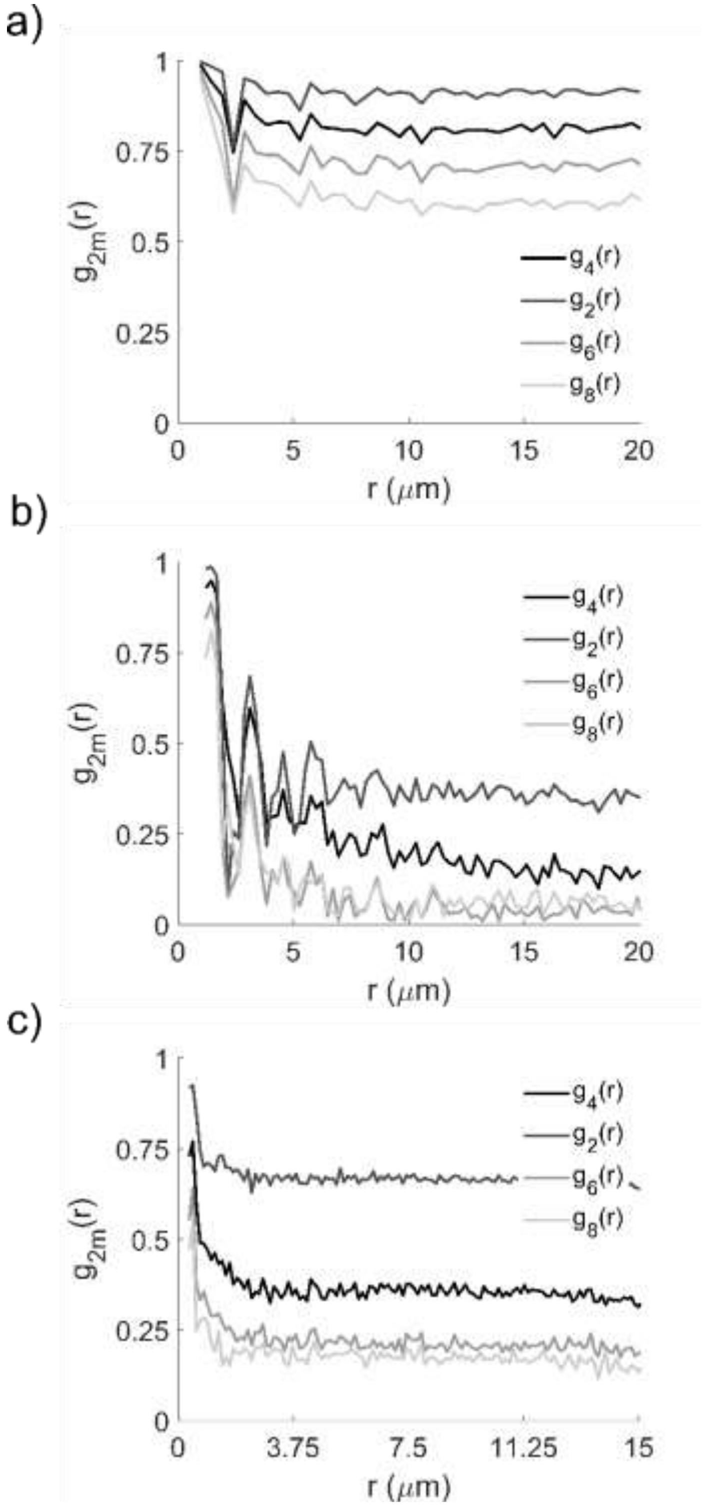

Figure 7: Orientational correlation functions g2m(r) for assemblies of fullerene microcrystal rods under two-dimensional confinement and electric field frequency greater than f_c. a) C_{60}-2 rods assembled at 3 MHz, 1.36 kV/cm, b) C_{60}-1.7 rods assembled at 3 MHz, 1.36 kV/cm, and c) C_{70}-3.9 rods assembled at 3.1 MHz, 1.23 kV/cm.

Table 1: Particle size statistics as calculated from SEM images. Reported uncertainties are standard deviations and the polydispersity index (PDI) is calculated for each dimension and the aspect ratio.

PARTICLE NAME	**LENGTH (μM)**	**WIDTH (μM)**	**ASPECT RATIO**
C_{60}-2	1.23 ± 0.05 (PDI 0.99)	0.61 ± 0.03 (PDI 0.99)	2.01 ± 0.13 (PDI 0.99)
C_{60}-1.7	1.46 ± 0.04 (PDI 0.99)	0.86 ± 0.04 (PDI 0.99)	1.70 ± 0.09 (PDI 0.99)
C_{70}-3.9	1.15 ± 0.05 (PDI 0.99)	0.29 ± 0.03 (PDI 0.98)	3.89 ± 0.46 (PDI 0.98)

Table 2: Nematic and tetratic order parameters for rod assemblies with and without electric fields. Area fraction is calculated using the particle dimensions calculated from SEM images and the number density of particles from the microscope images.

PARTICLE NAME	**FIELD**	**AREA FRACTION**	**AREA FRACTION (UNITLESS)**	**S_2**	**S_4**	**NEAREST NEIGHBOR DISTANCE (μM)**
C_{60}-2	No field		0.42	0.34	0.76	0.96
	$f < f_c$	High	0.48	0.24	0.82	1.44
	$f < f_c$	Moderate	0.30	0.32	0.88	1.44
	$f < f_c$	Low	0.54	0.51	0.94	1.44
	$f > f_c$		0.6	0.99	0.96	0.96
C_{60}-1.7	No field		0.55	0.25	0.45	1.0
	$f < f_c$	High	0.55	0.59	0.36	1.68
	$f < f_c$	Moderate	0.44	0.82	0.71	1.68
	$f < f_c$	Low	0.22	0.95	0.85	1.91
	$f > f_c$		0.58	0.71	0.62	1.44
C_{70}-3.9	No field		0.80	0.32	0.43	0.35
	$f < f_c$	High	0.89	0.82	0.64	0.35
	$f < f_c$	Moderate	0.71	0.85	0.69	0.47
	$f < f_c$	Low	0.49	0.99	0.97	0.35
	$\boldsymbol{f > f_c}$		0.52	0.88	0.73	0.48

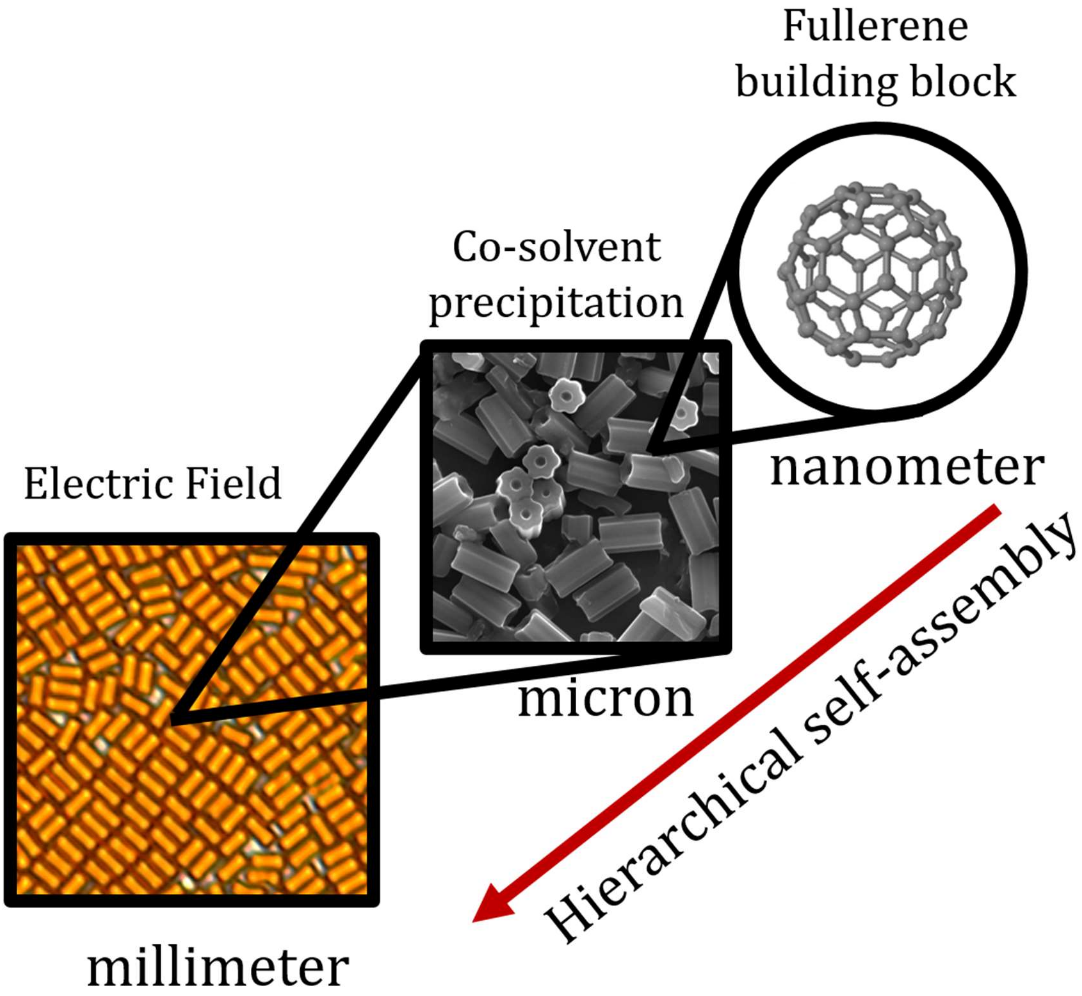
Fullerene
building block
Co-solvent
precipitation
Electric Field
nanometer
micron
millimeter
Hierarchical self-assembly